UNIVERSITY OF BIRMINGHAM
University of Birmingham Research at Birmingham

Numerical study of the solution heat treatment, forming, and in-die quenching (HFQ) process on AA5754

El Fakir, Omer; Wang, Liliang; Balint, Daniel; Dear, John P.; Lin, Jianguo; Dean, Trevor A.

DOI:
10.1016/j.ijmachtools.2014.07.008

License:
Creative Commons: Attribution (CC BY)

Document Version
Publisher's PDF, also known as Version of record

Citation for published version (Harvard):
El Fakir, O, Wang, L, Balint, D, Dear, JP, Lin, J & Dean, TA 2014, 'Numerical study of the solution heat treatment, forming, and in-die quenching (HFQ) process on AA5754', *International Journal of Machine Tools and Manufacture*, vol. 87, pp. 39-48. https://doi.org/10.1016/j.ijmachtools.2014.07.008

Link to publication on Research at Birmingham portal

Publisher Rights Statement:
Published under a Creative Commons Attribution license.

Eligibility for repository checked March 2015

General rights
Unless a licence is specified above, all rights (including copyright and moral rights) in this document are retained by the authors and/or the copyright holders. The express permission of the copyright holder must be obtained for any use of this material other than for purposes permitted by law.

•Users may freely distribute the URL that is used to identify this publication.
•Users may download and/or print one copy of the publication from the University of Birmingham research portal for the purpose of private study or non-commercial research.
•User may use extracts from the document in line with the concept of 'fair dealing' under the Copyright, Designs and Patents Act 1988 (?)
•Users may not further distribute the material nor use it for the purposes of commercial gain.

Where a licence is displayed above, please note the terms and conditions of the licence govern your use of this document.

When citing, please reference the published version.

Take down policy
While the University of Birmingham exercises care and attention in making items available there are rare occasions when an item has been uploaded in error or has been deemed to be commercially or otherwise sensitive.

If you believe that this is the case for this document, please contact UBIRA@lists.bham.ac.uk providing details and we will remove access to the work immediately and investigate.

Download date: 04. May. 2023

International Journal of Machine Tools & Manufacture 87 (2014) 39–48

Contents lists available at ScienceDirect

International Journal of Machine Tools & Manufacture

journal homepage: www.elsevier.com/locate/ijmactool

Numerical study of the solution heat treatment, forming, and in-die quenching (HFQ) process on AA5754

Omer El Fakir [a], Liliang Wang [a], Daniel Balint [a], John P. Dear [a], Jianguo Lin [a,*], Trevor A. Dean [b]

[a] Department of Mechanical Engineering, Imperial College London, London SW7 2AZ, UK
[b] School of Mechanical Engineering, The University of Birmingham, Edgbaston, Birmingham B15 2TT, UK

ARTICLE INFO

Article history:
Received 17 May 2014
Received in revised form
17 July 2014
Accepted 21 July 2014
Available online 1 August 2014

Keywords:
AA5754
FE process modelling
Constitutive equations
HFQ

ABSTRACT

An FE model of the solution heat treatment, forming and in-die quenching (HFQ) process was developed. Good correlation with a deviation of less than 5% was achieved between the thickness distribution of the simulated and experimentally formed parts, verifying the model. Subsequently, the model was able to provide a more detailed understanding of the HFQ process, and was used to study the effects of forming temperature and speed on the thickness distribution of the HFQ formed part. It was found that a higher forming speed is beneficial for HFQ forming, as it led to less thinning and improved thickness homogeneity.

© 2014 The Authors. Published by Elsevier Ltd. This is an open access article under the CC BY license (http://creativecommons.org/licenses/by/3.0/).

1. Introduction

Due to growing concerns about escalating energy prices and the contribution of CO_2 emissions to climate change, fuel efficiency has become the primary driver for technological advancements in road vehicles. Two potential routes to improving efficiency are powertrain optimization techniques and mass reduction. The body structure of an automobile constitutes around a quarter of its mass. By using lightweight materials such as aluminium alloys, this mass can be reduced by over 40%, leading to approximately a 32% increase in efficiency [1].

Currently, only 9% of an automobile's mass is composed of aluminium parts, which are predominantly cast. Significant research is now being undertaken to expand the use of aluminium into formed sheet parts, such as body panels and bumpers [1]. However, one of the major obstacles to using sheet aluminium alloys is their limited formability at room temperature, which is especially the case for the higher strength alloys [2]. In addition to work being done to develop alloys of improved formability [2], advanced forming technologies are also being investigated to form complex-shaped parts from these alloys.

Solution heat treatment, forming, and in-die quenching (HFQ) is one such technology [3]. In this process, the blank is first heated up to its solution heat treatment (SHT) temperature. At this elevated temperature, the solid solubility is increased and the alloying elements, or precipitates, fully dissolve into the aluminium matrix. Consequently the yield stress is reduced and the material becomes more ductile due to the fewer obstacles to dislocation movement [4], enabling more complex shapes to be formed. The blank is then transferred to a cold die, formed at a high speed and held in the cold tool to achieve a rapid cooling rate to room temperature. The fast pace of the process allows a supersaturated solid solution (SSSS) to be obtained [5]. This is a desirable microstructure that is extremely important for the post-form strength of a part, particularly if a heat treatable alloy is used. Valuable research work has been conducted on the effects of solutionising time and quenching rate on an HFQ formed part, which verified the high strength achievable following an appropriate ageing process [6,7]. Holding the formed part in the cold die after forming minimizes thermal distortion and springback due to the high cooling rate and lower material strength during forming.

The HFQ process hence presents an opportunity to expand the use of aluminium in complex-shaped sheet parts. However, it is essential that the correct combination of forming parameters, such as temperature, ram speed and blankholding force, are selected. Finite element (FE) process simulations are invaluable for determining and optimizing these parameters, and can reduce the efforts of experimental trials and hence lead times and costs, while ensuring a high quality final part [8–10]. The feasibility of new, unconventional metal forming processes can also be assessed by running FE simulations [11,12].

In recent years, efforts have been made to develop FE models capable of simulating sheet metal forming processes at elevated

* Corresponding author. Tel.: +44 20 7594 7082; fax: +44 20 7594 7017.
E-mail address: jianguo.lin@imperial.ac.uk (J. Lin).

http://dx.doi.org/10.1016/j.ijmachtools.2014.07.008
0890-6955/© 2014 The Authors. Published by Elsevier Ltd. This is an open access article under the CC BY license (http://creativecommons.org/licenses/by/3.0/).

temperatures accurately, using material models comprised of phenomenological or physically based equations calibrated using the results of uniaxial tension tests [12–15]. Tabular flow stress data can also be used to describe the material if a sufficient range of values is input, to prevent excessive extrapolation of the data and potentially inaccurate results [16]. A failure criterion is necessary to model the material behaviour upon the nucleation of damage and beyond the point of necking, to accurately simulate the later stages of the forming process [15,17]. For non-isothermal processes, coupled thermo-mechanical simulations are conducted using temperature dependent material models, to account for the heat transfer between the blank and the tool parts [18]. The interfacial heat transfer coefficient in such a process can be predicted accurately using numerical methods [19]. If the assumption can be made that the blank's temperature field is constant during the forming phase, then it may be calculated in a separate thermal simulation and then input in a purely mechanical simulation to save on computational time [20]. Friction models can also be implemented to improve the results of forming simulations of complex-shaped parts, by accounting for the viscosity of the lubricant used during forming and the surface roughness of the tooling and blank [21].

To verify the accuracy of the results of a simulation, most authors compared the numerical forming load/displacement curves with the experimental ones [16,22]. Further verification of and confidence in the results was achieved by comparing geometrical aspects of the numerically and experimentally formed parts, such as their draw depth in the case of a square cup drawing process [17], and their thickness distributions [14,23].

For the HFQ forming of the aluminium alloy AA5754 into a complex-shaped part, an FE simulation utilizing a physically based material model was run in ABAQUS. The development and application of this simulation is documented in this paper. Ductility and forming tests were first run to acquire data for calibrating the material model and for comparing against the results of the FE simulations, respectively. The viscoplastic damage constitutive equations of the model were then implemented via the user-defined subroutine VUMAT in ABAQUS. The use of a coupled thermo-mechanical simulation meant that the effect of non-uniform temperature could be captured. By comparison of the numerical thickness distribution data with the available experimental data from the forming tests, the results of the simulation were verified. The same simulation set-up could then be used to investigate more detailed aspects of the deformation and to predict part quality under different forming parameters.

2. Experimental details

2.1. Uniaxial tensile tests

Uniaxial tensile tests were conducted in a Gleeble 3800 thermo-mechanical testing system. This uses direct electrical resistance heating to heat specimens at rates of up to 10,000 °C/s. High cooling rates are also possible as the specimens are mounted in continuously cooled grips. Feedback control of the temperature is achieved via 2 thermocouple wires attached to the centre of the specimen.

The test-piece material AA5754 was supplied by Novelis UK Ltd in the form of $400 \times 400 \times 1.5$ mm^3 sheet, in the H111 condition. The composition of the material, provided by the supplier, is shown in Table 1.

The sheet material was machined into dog-bone shaped tensile specimens using climb milling to achieve a good quality finish; Fig. 1 shows the design and associated dimensions.

Table 1
The chemical composition of AA5754.

Element	Si	Fe	Cu	Mn	Mg	Cr	Zn	Ti	Al
Wt%	0.08	0.16	0.004	0.45	3.2	0.001	0.01	0.02	Bal.

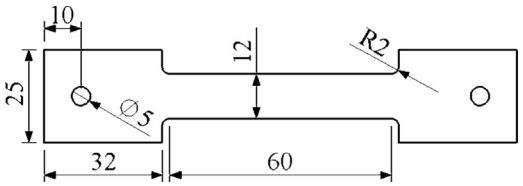

Fig. 1. Gleeble test specimen dimensions.

Due to the possibility of overheating, specimens were first heated to a temperature of 25 °C lower than the target temperature at a heating rate of 50 °C/s, and then further heated to the target temperature at a rate of 5 °C/s. They were soaked at this temperature for 1 min, and then deformed, to ensure a homogeneous temperature distribution. After deformation, they were cooled down to room temperature by conduction with the cool grips. Fig. 2 shows the temperature evolution with time. The test chamber was maintained at room temperature and pressure throughout the tests.

Different temperatures between 20 °C and 550 °C, and strain rates between 0.1 and 10 s^{-1}, were tested. The results of these tests were used to calibrate the constitutive equations.

2.2. Forming tests

The forming tests on the alloy were conducted using the HFQ process on an existing tool for producing stiffener components, designed in the authors' laboratory and manufactured by a die-maker. The results of the tests could be used to verify the simulation set-up for the HFQ process.

The tool used, shown in Fig. 3, was mounted onto a 250 kN ESH press which provided the forming load. The test specimen was first heated in a furnace to the target temperature, monitored using a thermocouple wire attached to it, and then quickly and carefully placed in the tool for 10 s, which stamped the specimen when the press was activated. As the load was applied, the top blankholder was displaced downwards, compressing the 1st stage blankholding force (BHF) springs. With the blank held between the top and bottom blankholders, the top die deformed the blank further towards the bottom die, engaging the 2nd stage BHF gas springs. The formed part was then held in the cold die after forming to quench it to room temperature. Subsequently the load was removed and the ejector springs separated the blankholders, enabling removal of the part. Further details about the process are provided in Section 3.1. The die, blankholders and punches of the tool were lubricated before each test using Stuart lubricating oil supplied by Houghton plc.

Forming tests were conducted at a speed of 250 mm/s and at temperatures of 200 and 350 °C, in addition to the HFQ temperature of 480 °C. These test conditions would provide sufficient data points for comparison with the numerical results. An example of a fully formed part is shown in Fig. 4a, with the flanges trimmed off.

For the purposes of this investigation, only a section of the full part with dimensions of 200×65 mm^2 was formed, as shown in Fig. 4b. This helped to avoid the difficulty of having to optimize the blank shape to form a successful part for each forming condition, while encompassing the most complex features of the part.

3. FE modelling of HFQ forming process

3.1. FE model set-up

An FE model of the HFQ forming process was created using ABAQUS. Geometry models of the relevant tool parts generated in CAD software were imported into the FE code (Fig. 5). The dimensions of the blank were the same as those used in the forming tests ($200 \times 65 \times 1.5\ mm^3$), and the position of the blank on the bottom blankholder was kept consistent with the experiments. A 3D simulation was selected due to the lack of symmetries and the complex shape of the formed part.

An explicit solver was run, due to its robustness in handling a frictional contact problem as compared to an implicit solver [8]. For the blank, explicit, 8-node thermally coupled brick elements (C3D8T), with 3 degrees of freedom in both displacement and temperature, were used to accurately represent the deformation and heat transfer mechanisms that occur during the HFQ process. To improve the accuracy of the simulation and to capture the effects of bending and stretching, five elements were used in the thickness direction of the blank. The selected element size ($1 \times 1 \times 0.3\ mm^3$) ensured that the deformation of the central features could be captured accurately while maintaining an acceptable computational time.

For the tool parts, to avoid the very high mesh resolutions required to capture their complex geometries, explicit, 4-node thermally coupled tetrahedron elements (C3D4T), linear in displacement and temperature, were selected. Both the blank and the tool parts were set as deformable bodies in order to model the heat transfer between them. Therefore to avoid long simulation times, a coarser resolution was chosen for the tools, since deformation of these parts was not of interest, but only their heat transfer characteristics.

Encastre boundary conditions were used for the bottom punches and bottom blankholder, to restrict all degrees of freedom. For the top punch and bottom die, as well as the top blankholder, all degrees of freedom, except for that in the vertical direction (the punch axis), were restricted. In the actual tool, guide pillars ensure that these parts only move vertically. Fig. 6a shows the tooling and blank just before forming is initiated. During the forming process, the blank is formed in two continuous stages: the draw-in (1st) stage and the deep drawing (2nd) stage. In the 1st stage, the general shape of the part is formed (Fig. 6b) as the top punch makes contact with the blank and deforms it towards the bottom die, forming the central recess of the part. In the 2nd stage, the central features of the part are formed (Fig. 6c) as the bottom die and blank are displaced further down onto the bottom punches. The 1st stage blankholding force (BHF) was provided by a uniform pressure applied onto the surface of the top blankholder, while in the 2nd stage an additional BHF was provided by a spring fixed to the bottom die of stiffness equal to that of the gas springs used in the tool. The forming was initiated by displacing the top punch downwards towards the blank at the required speed.

The tool material was specified as H13 steel and assigned a very high stiffness to prevent it from deforming; only the heat transfer to it from the blank was of interest. For the blank, a user-defined material subroutine for the alloy AA5754 was implemented to achieve an accurate representation of its deformation at different temperatures. The subroutine was essential for modelling the non-isothermal conditions of the HFQ process. The effects of the change in temperature of the blank on its deformation response (due to heat transfer with the tooling) were captured by the material model, which contains temperature-dependent constants.

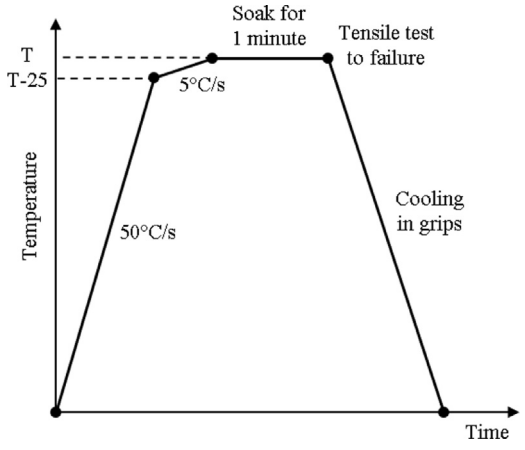

Fig. 2. Programmed temperature evolution for the Gleeble tests.

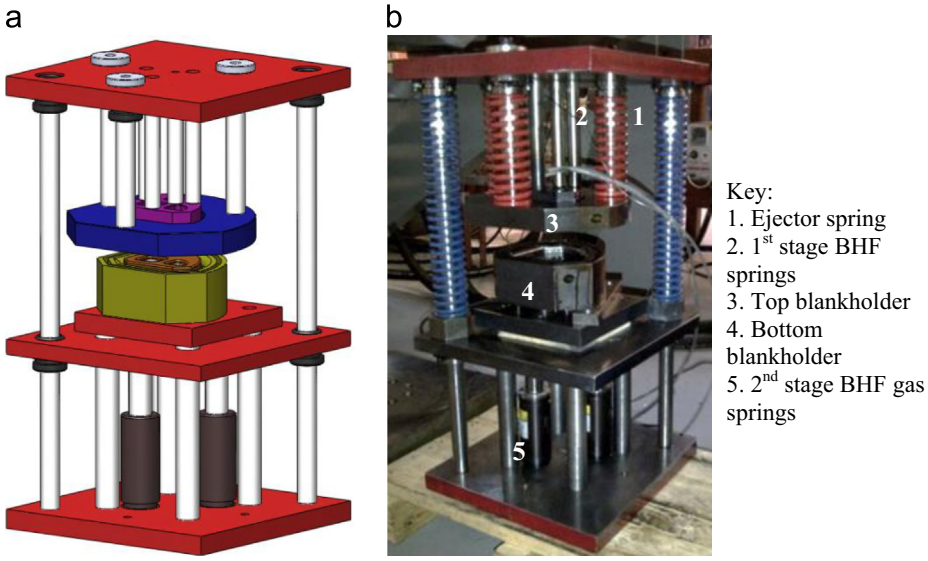

Fig. 3. (a) SolidWorks model and (b) photograph of the stamping tool used.

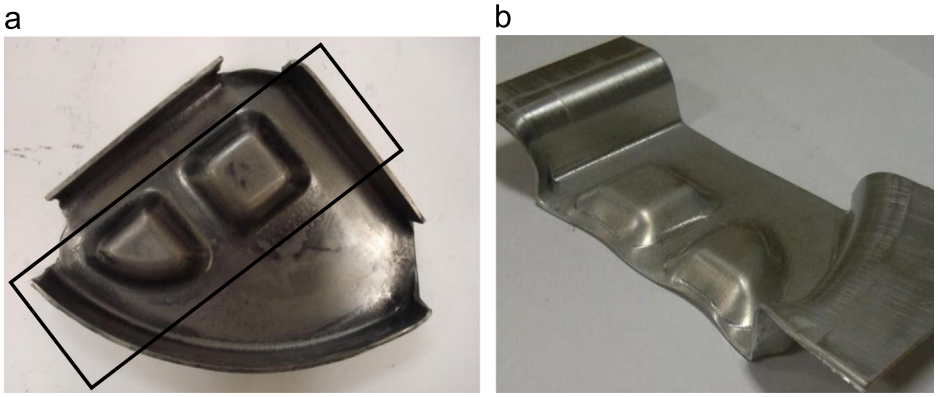

Fig. 4. (a) Fully formed and trimmed part and (b) section formed, highlighted by rectangle in (a).

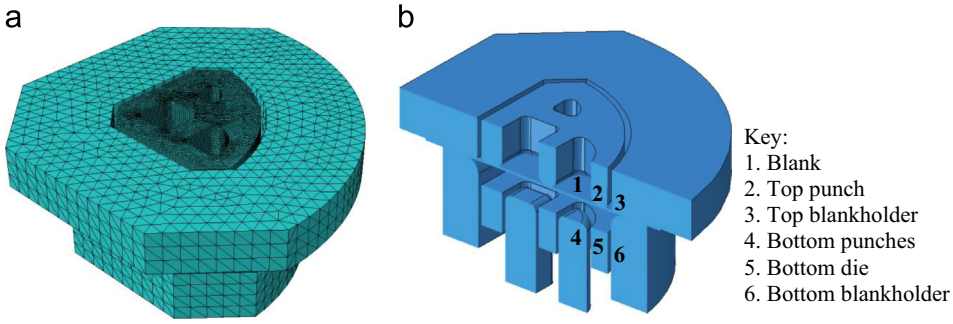

Fig. 5. (a) Meshed view and (b) sectioned view of the tool part assembly used.

The physical properties of the blank and tooling material are shown in Table 2, and the main parameters of the simulation are shown in Table 3. The values selected for the friction and heat transfer coefficient were based on previous work done by Foster et al. [24].

The simulation results were verified by comparing thickness distributions across a section of the part, as complete strain information was not available from the experimentally formed parts. Hence for the purposes of this work, the quenching stage of the process was not simulated as it would not affect thickness homogeneity.

3.2. Material model for AA5754

AA5754 is a non-heat treatable aluminium alloy, and its strength is achieved through solid solution hardening by the magnesium (Mg) atoms in the aluminium lattice, as well as strain hardening [25]. At elevated temperatures, strain rate and temperature both affect the deformation properties. When heated to its SHT temperature of 480 °C during the HFQ process, excess Mg atoms present in the alloy dissolve into the primary α-Al matrix, enabling much greater formability.

The constitutive equations developed for the aluminium alloy AA5754 were implemented in the FE code through the user-defined material subroutine VUMAT. The deformation response is comprised of two mechanisms: viscoplasticity occurs throughout the deformation process, and damage in the latter stages of deformation [26].

The flow rule selected for this material incorporates thermally activated mechanisms in addition to the effect of plastic deformation by dislocation motion; hence the flow stress is a function of both the plastic strain and the plastic strain rate:

$$\sigma = K\varepsilon_P^N \dot{\varepsilon}_P^m \tag{1}$$

where 'K' is a temperature-dependent material constant, 'N' is the strain-hardening exponent and 'm' is the strain-rate hardening exponent [27]. Eq. (1) was rearranged to form the viscoplastic flow rule:

$$\dot{\varepsilon}_P = (\sigma/K\varepsilon_P^N)^{1/m} \tag{2}$$

Eq. (2) was then modified such that the viscoplastic material flow was expressed solely in terms of the stress potential that can contribute to it. An initial dynamic yield point, 'k', was introduced, as well as the variable 'R', which represents the isotropic hardening of the material due to dislocation entanglements and pile-ups, and both reduce the plastic strain potential. The reduction in the effective load-bearing cross-sectional area of the material due to damage 'ω' was also accounted for by assuming that the stress was applied over the undamaged area:

$$\dot{\varepsilon}_P = (\sigma/(1-\omega) - R - k/K)^{n_1} \tag{3}$$

where K and n_1 are temperature-dependent material constants [26].

The isotropic hardening variable 'R' is a function of the normalized dislocation density in the material, and was postulated by Garrett et al. as follows [4]:

$$\dot{R} = 0.5B\overline{\rho}^{-0.5}\dot{\overline{\rho}} \tag{4}$$

where 'B' is a temperature dependent material constant, and '$\overline{\rho}$' is the normalized dislocation density. As the dislocation density increases, there is a proportional increase in the hardening variable, since a greater stress is required to continue deformation.

A normalized form of the dislocation density was used, which varies from 0 in the initial state, to 1 in the saturated state. The expression for its evolution takes the form:

$$\dot{\overline{\rho}} = A(1-\overline{\rho})|\dot{\varepsilon}_P| - C\overline{\rho}^{n_2} \tag{5}$$

where 'A' and 'C' are temperature-dependent material constants [27]. The first term of Eq. (5) represents the accumulation of dislocations

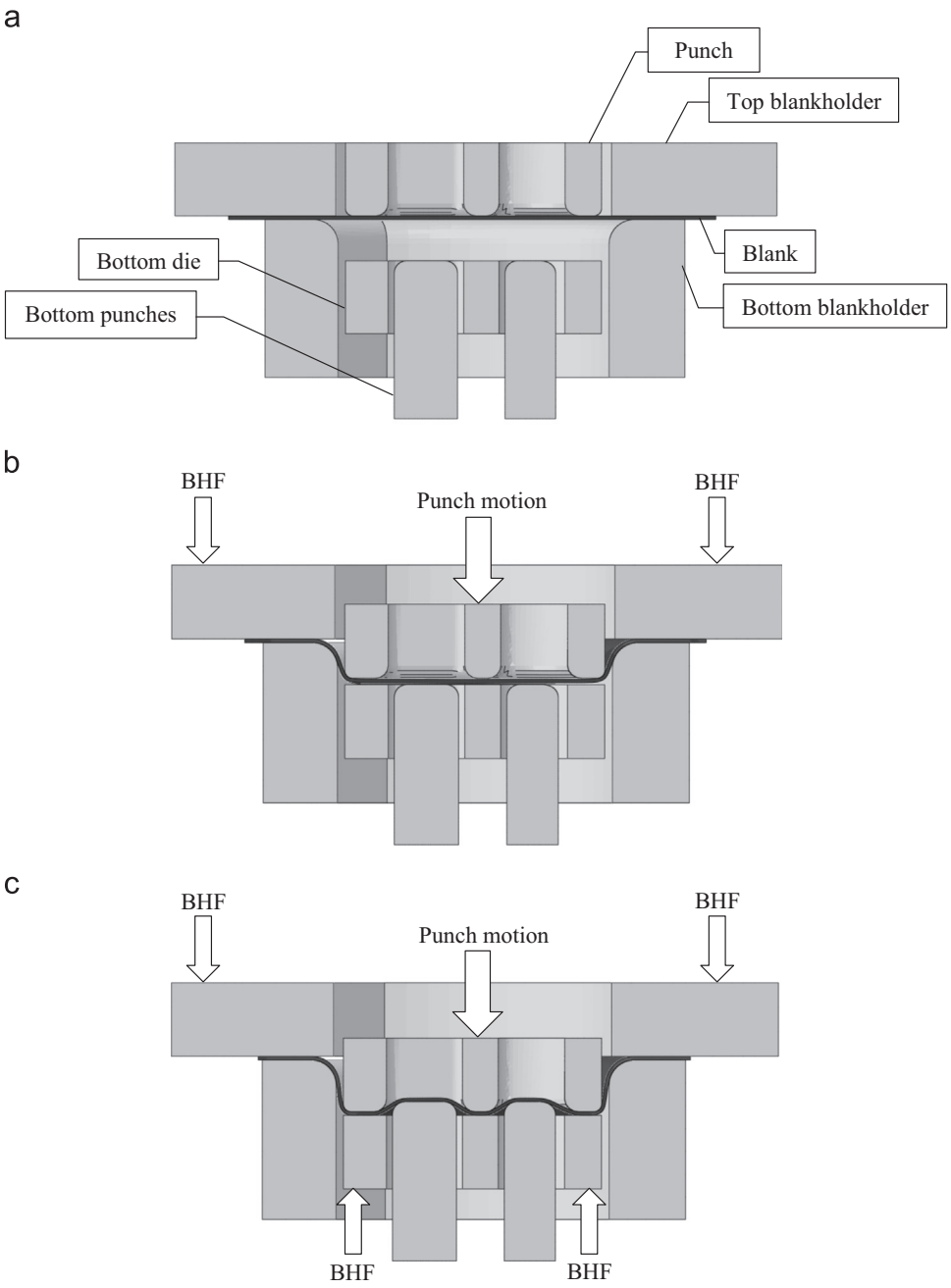

Fig. 6. (a) Labelled section of the tooling and blank, (b) the 1st stage of the forming process, where the blankholding force (BHF) is provided by the top blankholder, and (c) the 2nd stage, where the blank makes contact with the bottom die and a BHF is also applied by the gas springs.

Table 2
Material properties of workpiece and tooling.

Property	AA5754	H13 tool steel
Thermal conductivity (kW/mm K)	147	38
Specific heat (mJ/tonne K)	9.6E8	4.7E8
Density (tonne/mm^3)	2.7E−9	7.8E−9
Poisson's ratio	0.33	0.3
Young's modulus (MPa)		2.1E5

Table 3
Main process and simulation parameters.

Initial workpiece temperature (°C)	200, 350, 480
Initial tooling temperature (°C)	20
Ram speed (mm/s)	250, 500, 750
Number of elements	581,996
Friction coefficient	0.1
Heat transfer coefficient (kW/mm^2 K)	4.31

due to plastic flow and dynamic recovery, and the second term represents static recovery. At low temperatures, dislocation drag is caused by the magnesium solute atoms, reducing the rate of dynamic recovery and increasing the dislocation density, hence hardening the alloy and decreasing ductility [28]. When formed at elevated temperatures, diffusion of the solutes enables rearrangement of the dislocations, increasing the rate of dislocation annihilation through dynamic recovery and decreasing their density. The alloy is more ductile as a result.

In the later stages of deformation, the material response becomes dictated by damage evolution in addition to

viscoplasticity. The form of the damage evolution equation used for AA5754 was based on the growth and nucleation of voids around particles:

$$\dot{\omega} = \eta_1/(1-\omega)^{\eta_2}(\sigma\dot{\varepsilon}_P^{\eta_3}) \tag{6}$$

where 'ω' is the damage parameter, defined as the area fraction of damaged material, and 'η_1', 'η_2' and 'η_3' are temperature-dependent material constants [26]. Eq. (6) is a modified version of the expression set out by Khaleel et al. for damage due to superplastic void growth [29], which is appropriate for this case where the fine grained alloy is deformed excessively at high temperatures; however only the later stage damage was of interest here.

The flow stress equation was modified to include the effect of damage and is as follows:

$$\sigma = E(1-\omega)(\varepsilon_T - \varepsilon_P) \tag{7}$$

where 'E' is Young's modulus of the material, and is temperature-dependent.

Contained within these equations are numerous temperature-dependent material constants. The equations for these, which take the form of Arrhenius equations, are as follows:

$$K = K_0 \exp\left(\frac{Q_K}{RT}\right) \tag{8}$$

$$k = k_0 \exp\left(\frac{Q_k}{RT}\right) \tag{9}$$

$$B = B_{0_1}\left(\frac{1}{T}\right)^{B_{0_2}} \tag{10}$$

$$C = C_0 \exp\left(\frac{-Q_C}{RT}\right) \tag{11}$$

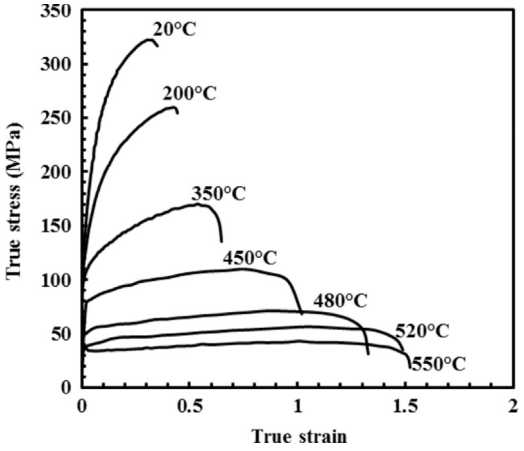

Fig. 7. Uniaxial tension test results of AA5754 at different temperatures at a strain rate of 1/s.

$$E = E_0 \exp\left(\frac{Q_E}{RT}\right) \tag{12}$$

$$\eta_1 = \eta_{0_1} \exp\left(\frac{-Q_{\eta_1}}{RT}\right) \tag{13}$$

$$\eta_2 = \eta_{0_2} \exp\left(\frac{Q_{\eta_2}}{RT}\right) \tag{14}$$

$$\eta_3 = \eta_{0_3} \exp\left(\frac{-Q_{\eta_3}}{RT}\right) \tag{15}$$

$$A = A_0 \exp\left(\frac{-Q_A}{RT}\right) \tag{16}$$

$$n_1 = n_{0_1} \exp\frac{Q_{n_1}}{RT} \tag{17}$$

The equations outlined above were calibrated using the experimental data from the uniaxial tension test results at different temperatures and strain rates for AA5754. The results of the tests for a strain rate of 1/s show a trend of decreasing strength and increasing ductility with increasing temperature, as shown in Fig. 7. The highest ductilities were achieved at temperatures greater than 480 °C, which is the SHT temperature of the material.

The 21 different material constants contained within the equation set were determined by fitting the equations to the experimental data using optimization techniques [30]. The range of possible values for the constants was defined based on their physical meanings and from experience. The constants are listed in Table 4. A comparison between the stress–strain behaviour predicted by the material model and that obtained from the tensile tests is shown in Fig. 8.

4. Results and discussion

4.1. FE model verification

The FE model developed in ABAQUS was verified by comparing the numerical results with the experimental results. As can be seen from Fig. 9, in which the part was formed at a temperature and speed of 480 °C and 250 mm/s, the simulated part was geometrically accurate, having a near perfect match with the experimentally formed part.

Fig. 9b shows that the highest plastic strains occurred at the corner regions of the part, with the maximum value being approximately 78%, where localized thinning took place. To verify the numerical accuracy of the simulation, the normalized thickness distribution (t/t_0) across a section of the part containing the most corner features was measured manually using digital callipers, and compared with the thickness distribution across the same section from the simulated part.

Table 4
Material constants determined from calibration.

E_0 (MPa)	C_0 (S^{-1})	B_{0_1} (MPa)	k_0 (MPa)	K_0 (MPa)	η_{0_1} (dimensionless)	η_{0_2} (dimensionless)
13,211	217.8	6.75E+18	3.3932	0.0846	0.03203	1.7211
Q_E (J/mol)	Q_C (J/mol)	Q_k (J/mol)	Q_K (J/mol)	Q_{η_1} (J/mol)	Q_{η_2} (J/mol)	Q_{η_1} (J/mol)
6669.49	60,999.8	11,181.5	34,630.3	26,837.6	17,594.1	12,993
η_{0_3} (dimensionless)	Q_{η_3} (J/mol)	A_0 (dimensionless)	Q_A (J/mol)	n_2 (dimensionless)	n_{0_1} (dimensionless)	B_{0_2}
4.381	9469.6	1.9996	2898.3	0.3	3.56E−01	6.005

In Fig. 10a, the simulated profile was superposed on an image of the same section from the part shown in Fig. 9b, showing a good match between both profiles. A comparison between the numerical and experimental normalized thickness distribution, represented by a solid line and symbols respectively, is also shown in Fig. 10a.

Normalized thickness was calculated using

$$\hat{t} = t/t_0 \tag{18}$$

where 't' is the final thickness value, 't_0' the initial thickness and '$\hat{t}$' the normalized thickness.

The dashed lines between the figures indicate the location of the corner regions of the part and their corresponding normalized thickness. These regions exhibited the greatest amount of localized thinning. The maximum thinning percentage, calculated using Eq. (19), was approximately 16%, and occurred at the corner regions between the two central features, located at 84 and 96 mm along the section.

$$e_t = (1-\hat{t}) \times 100 \tag{19}$$

where '$\hat{t}$' is the normalized thickness and 'e_t' the thinning value.

Fig. 11 shows the temperature evolution during HFQ forming across the same section as above. A highly non-uniform temperature distribution can be observed. At the end of the 1st stage of forming, the areas of the blank labelled 'B' where the central features were formed were at a higher temperature than the surrounding area (labelled 'A'), which was quenched by the cold top punch (Part no. 2 in Fig. 5b) and bottom die (Part no. 5 in Fig. 5b). This can clearly be seen in Fig. 11 where these cooler areas correspond to the distance ranges 30–50, 85–95, and 130–145 mm along the section.

In the 2nd stage of the forming process, the central feature regions were hotter and more ductile, thus weaker than the surrounding areas. As a result less material was drawn-in and more plastic deformation occurred to form these features, which are located in the distance ranges 50–85 and 95–130 mm along the section in Figs. 10a and 11. Thinning was hence more severe (6–8%) here, compared to the surrounding material where it was less than 4%. This also explains why maximum thinning occurred in the corner regions between the central features mentioned previously, i.e. a combination of the temperature inhomogeneity and the lack of material drawing inbetween the two features resulted in a much higher level of plastic deformation. The same trends were observed for the parts formed at 350 °C and 200 °C. Their numerical and experimental normalized thickness distributions are shown in Figs. 10b and 10c, respectively.

Fig. 10 clearly shows that there were good agreements between the numerical and experimental results at the three different temperatures, with a deviation of less than 5% from the experimental results in all cases, in terms of the location and magnitude of localized thinning. The FE model has correctly predicted the quality of a part formed using the HFQ process, verifying the simulation set-up and constitutive equations. The same model could therefore be used to investigate the deformation of the material during HFQ forming in more detail, as well as the effects of the forming parameters on the final part.

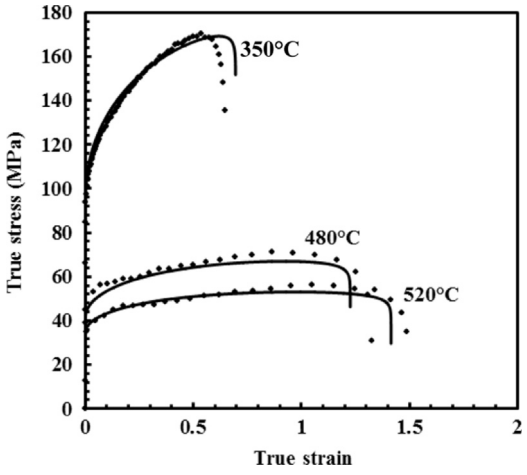

Fig. 8. Comparison of experimental (symbols) and computed (curves) at temperatures of 350, 480 and 520 °C at a strain rate of 1/s.

4.2. Effect of temperature on the thickness distribution

Fig. 12 shows a comparison between the simulated thickness distributions for the temperatures 200, 350 and 480 °C, at the forming speed of 250 mm/s. The effects of temperature on the thickness distribution were evaluated in terms of overall thinning, by calculating the mean of the thinning values across the section using Eq. (20), and thickness homogeneity, by calculating the standard deviation of the thickness values across the section using Eq. (21).

$$\bar{e}_t = \sum_{i=1}^{n} e_{ti}/n \tag{20}$$

where 'e_{ti}' is the thinning value, 'n' the sample size and '$\bar{e}_t$' the mean thinning.

$$\Delta = \sqrt{\sum_{i=1}^{n}(t_i-\hat{t})^2/(n-1)} \tag{21}$$

where 't_i' is the thickness value, '$\bar{t}$' the mean thickness, 'n' the sample size, and 'Δ' the standard deviation of the thickness values across the section.

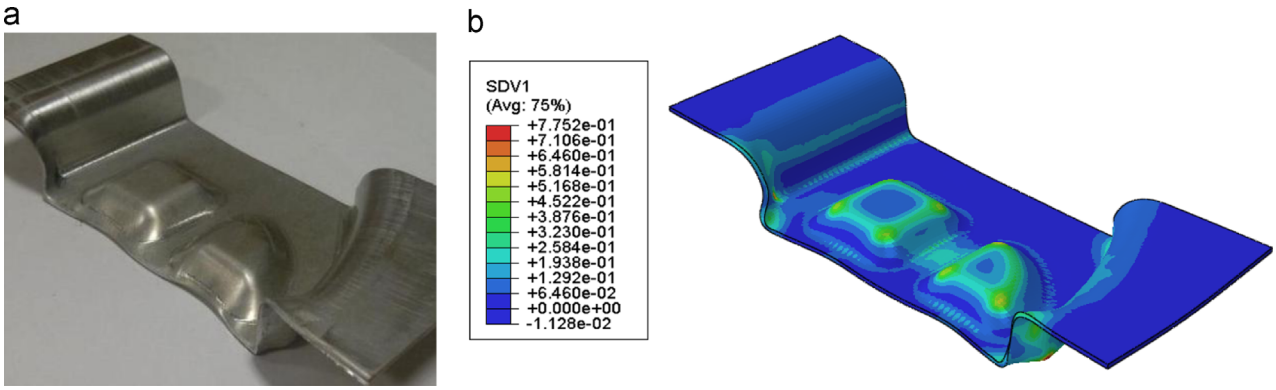

Fig. 9. (a) Successfully formed part, and (b) simulated part with plastic strain contour displayed.

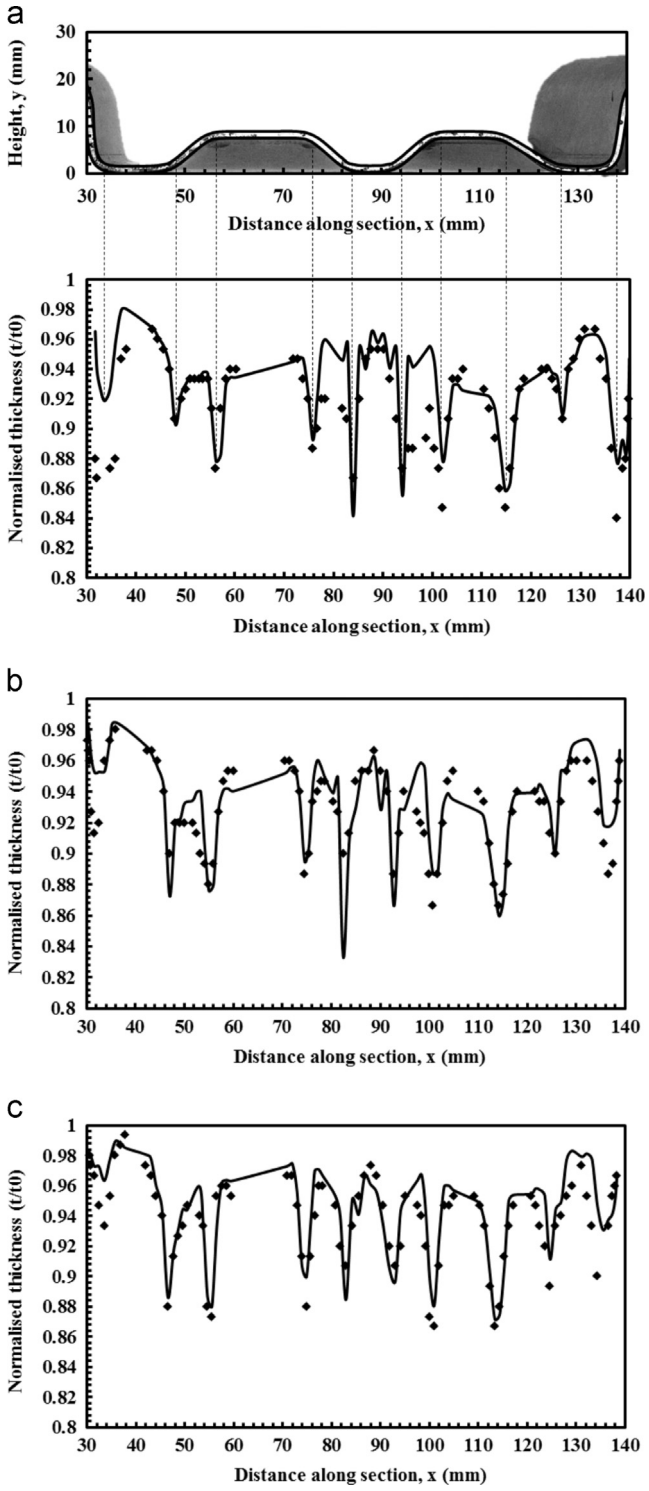

Fig. 10. Comparison between predicted (curves) and experimental (symbols) thickness distributions of the part formed at (a) 480 °C, (b) 350 °C and (c) 200 °C, at a forming speed of 250 mm/s.

The FE model correctly predicted that the least amount of overall thinning occurred in the part formed at 200 °C, while the one formed at 480 °C showed the greatest. The overall thinning at 200 °C was 5.4%. This increased to 6.5% at 350 °C, and 7.4% at 480 °C. Under HFQ conditions, the material is weaker and hence more ductile, limiting material draw-in. At lower temperatures, the material is stronger, and the strain hardening effect is greater. Hence under the same blankholding force, more material was drawn into the central recess of the part, and consequently plastic deformation and thinning were lower.

The thickness homogeneity was improved at lower temperatures. For the temperatures 200, 350 and 480 °C, the standard deviation was 0.044 mm, 0.045 mm and 0.048 mm, respectively. As the areas of the blank formed in the second stage of the process were more heavily deformed than those in the first stage, the strain hardening effect was more pronounced here, particularly at lower temperatures. The higher strength would facilitate more material draw-in, reducing the extent of plastic deformation; as such homogeneity is improved at lower temperatures.

It should be noted that the extent of localized thinning at the corner regions was similar for all temperatures. Despite more plastic deformation occurring at higher temperatures, the strain rate sensitivity was also higher; this reduced the extent of localized thinning to a level comparable to that seen at lower temperatures.

4.3. *Effect of forming speed on the thickness distribution*

Further simulations were carried out to extend the use of the model to the prediction of part quality under other forming conditions. Currently, only the effect of varying the forming speed was investigated, under HFQ conditions (at a blank temperature of 480 °C).

The variation in the thickness distribution across the same section as before for speeds of 250, 500 and 750 mm/s is shown in Fig. 13. The effects of forming speed on the thickness distribution were evaluated with regard to overall thinning and thickness homogeneity, calculated using Eqs. (20) and (21) respectively. The trend of thickness distribution was the same for all speeds. The overall thinning was 7.4%, 7.2% and 6%. Hence thinning decreased with increasing forming speed. At higher speeds, the material was deformed at a faster strain rate; hence the strain hardening effect was greater and the material being deformed was stronger. In addition to this, the higher speed meant there was less time for heat transfer between the hot blank and the cold blankholder; the material there remained hot and soft, compared to the stronger material being formed into the central recess of the part. More material was therefore drawn into the die, reducing the extent of plastic deformation.

For the speeds of 250 and 500 mm/s, the standard deviation of the thickness values across the section was approximately 0.048 mm, while for the highest speed of 750 mm/s it decreased to 0.042 mm. The thickness homogeneity was hence improved at this condition, due to two factors. Firstly the higher forming speed led to a reduction in the contact time between the top punch and the blank. Hence the area of the blank formed in the first stage of the process was hotter and softer compared to slower speeds. Secondly, as the blank was deformed faster, the strain hardening effect would have been greater, particularly for the regions of the blank that are formed into the complex shape of the central features. The combined effect of both factors led to greater material draw-in at higher forming speeds, reducing the level of thinning.

5. Conclusion

A coupled thermo-mechanical simulation of the HFQ forming of a complex-shaped part, integrating a calibrated user-defined material subroutine for the Al alloy AA5754, was successfully set up in the commercial FE software ABAQUS, and subsequently used to obtain a more detailed understanding of the HFQ process. The unified viscoplastic damage constitutive equations of the material model were calibrated using the results of uniaxial tensile test

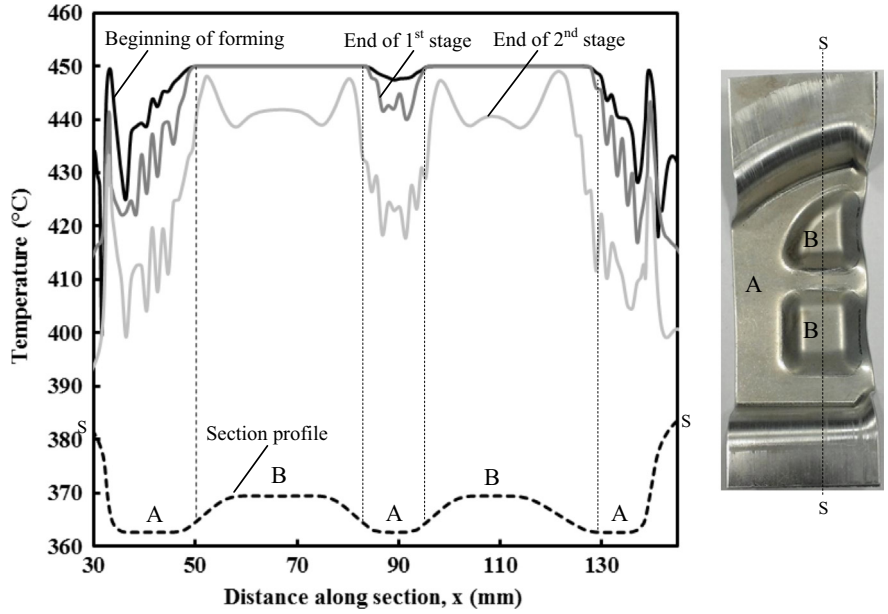

Fig. 11. Temperature distribution through section S-S at different stages of the forming process.

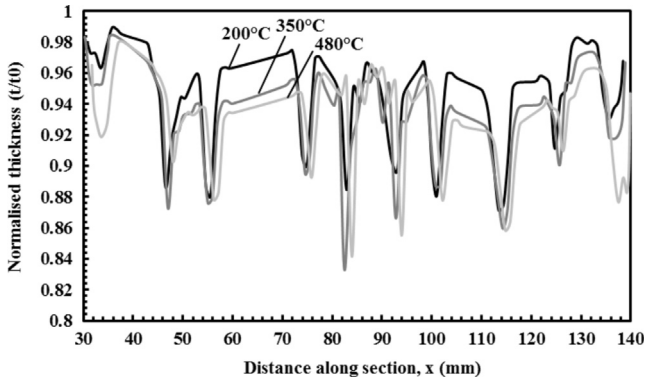

Fig. 12. Numerical thickness distributions across part section for different temperatures.

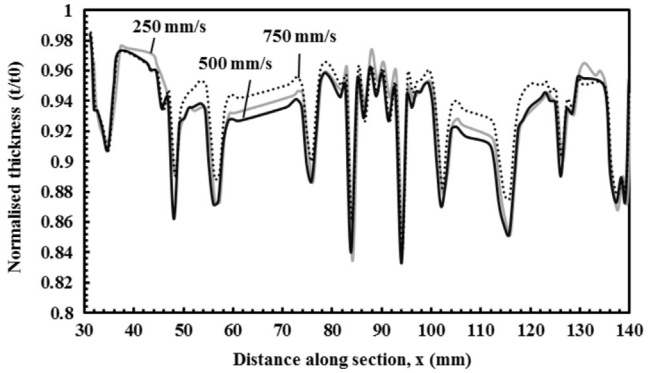

Fig. 13. Numerical thickness distributions across part section for different forming speeds.

data. The accuracy of the FE model was then verified by comparing the numerical and experimental geometry and thickness distributions across a section of the formed part. There was a very close geometric match and a good agreement between the thickness distribution results, with a deviation of less than 5% from the experimental results, validating the use of alloy-specific material models in process simulations. The developed FE model could then be used to analyse the effect of varying the blank temperature and forming speed on the thickness distribution of a part formed using the HFQ process.

It was found that overall thinning decreased and thickness homogeneity improved when the blank was formed at a lower temperature. As the blank temperature was decreased from 480 to 200 °C, the overall thinning decreased from 7.4% to 5.4%, and the standard deviation in the thickness decreased from 0.048 to 0.044 mm. For the forming speed, as it was increased from 250 to 750 mm/s, overall thinning decreased from 7.4% to 6%, and the standard deviation in the thickness decreased from 0.048 to 0.042 mm, indicating improved thickness homogeneity. It was concluded that higher forming speeds are beneficial for the HFQ forming of sheet parts. The greater strain hardening of the material at a higher forming speed would reduce the extent of localized thinning that occurs when forming it at the SHT temperature, yielding a part with minimal thinning in addition to a high post-form strength potential.

Acknowledgements

The authors gratefully acknowledge the support from the EPSRC (Grant Ref: EP/I038616/1) for TARF-LCV: Towards Affordable, Closed-Loop Recyclable Future Low Carbon Vehicle Structures.

References

[1] N.P. Lutsey, Review of technical literature and trends related to automobile mass-reduction technology, Institute of Transportation Studies, University of California, Davis, 2010.
[2] W.S. Miller, L. Zhuang, J. Bottema, A. Wittebrood, P. De Smet, A. Haszler, A. Vieregge, Recent development in aluminium alloys for the automotive industry, Mater. Sci. Eng. A Struct. Mater. Prop. Microstruct. Process. 280 (2000) 37–49.
[3] J. Lin, T.A. Dean, R.P. Garrett, F.A.D., A process in forming high strength and complex-shaped Al-alloy sheet components, in: British Patent, UK, 2008.
[4] R.P. Garrett, J. Lin, T.A. Dean, An investigation of the effects of solution heat treatment on mechanical properties for AA 6xxx alloys: experimentation and modelling, Int. J. Plast. 21 (2005) 1640–1657.
[5] M.F. Ashby, Engineering Materials 2: An Introduction to Microstructures, Processing and Design, 3rd Ed., Elsevier Butteworth-Heinemann, Oxford, 2006.

[6] X. Fan, Z. He, S. Yuan, K. Zheng, Experimental investigation on hot forming–quenching integrated process of 6A02 aluminum alloy sheet, Mater. Sci. Eng. A 573 (2013) 154–160.
[7] X.B. Fan, Z.B. He, S.J. Yuan, P. Lin, Investigation on strengthening of 6A02 aluminum alloy sheet in hot forming-quenching integrated process with warm forming-dies, Mater. Sci. Eng. A: Struct. Mater. Prop. Microstruct. Process. 587 (2013) 221–227.
[8] M. Firat, Computer aided analysis and design of sheet metal forming processes: Part I – The finite element modeling concepts, Mater. Des. 28 (2007) 1298–1303.
[9] M. Firat, Computer aided analysis and design of sheet metal forming processes: Part II – Deformation response modeling, Mater. Des. 28 (2007) 1304–1310.
[10] M. Tisza, Numerical modelling and simulation in sleet metal forming, J. Mater. Process. Technol. 151 (2004) 58–62.
[11] J.L. Chenot, E. Massoni, Finite element modelling and control of new metal forming processes, Int. J. Mach. Tools Manuf. 46 (2006) 1194–1200.
[12] Q.-F. Chang, D.-Y. Li, Y.-H. Peng, X.-Q. Zeng, Experimental and numerical study of warm deep drawing of AZ31 magnesium alloy sheet, Int. J. Mach. Tools Manuf. 47 (2007) 436–443.
[13] T. Meinders, E.S. Perdahcıoğlu, M. van Riel, H.H. Wisselink, Numerical modeling of advanced materials, Int. J. Mach. Tools Manuf. 48 (2008) 485–498.
[14] M.S. Mohamed, A.D. Foster, J.G. Lin, D.S. Balint, T.A. Dean, Investigation of deformation and failure features of AA6082: experimentation and modelling, Int. J. Mach. Tools Manuf. 53 (2012) 27–38.
[15] R. Verma, L.G. Hector, P.E. Krajewski, E.M. Taleff, The finite element simulation of high-temperature magnesium AZ31 sheet forming, JOM 61 (2009) 29–37.
[16] H. Palaniswamy, G. Ngaile, T. Altan, Finite element simulation of magnesium alloy sheet forming at elevated temperatures, J. Mater. Process. Technol. 146 (2004) 52–60.
[17] F.-K. Chen, T.-B. Huang, C.-K. Chang, Deep drawing of square cups with magnesium alloy AZ31 sheets, Int. J. Mach. Tools Manuf. 43 (2003) 1553–1559.
[18] S. Kurukuri, A.H. van den Boogaard, A. Miroux, B. Holmedal, Warm forming simulation of Al–Mg sheet, J. Mater. Process. Technol. 209 (2009) 5636–5645.
[19] Q. Bai, J. Lin, L. Zhan, T.A. Dean, D.S. Balint, Z. Zhang, An efficient closed-form method for determining interfacial heat transfer coefficient in metal forming, Int. J. Mach. Tools Manuf. 56 (2012) 102–110.
[20] G. Palumbo, D. Sorgente, L. Tricarico, The design of a formability test in warm conditions for an AZ31 magnesium alloy avoiding friction and strain rate effects, Int. J. Mach. Tools Manuf. 48 (2008) 1535–1545.
[21] T.-S. Yang, The strain path and forming limit analysis of the lubricated sheet metal forming process, Int. J. Mach. Tools Manuf. 47 (2007) 1311–1321.
[22] N. Abedrabbo, F. Pourboghrat, J. Carsley, Forming of AA5182-O and AA5754-O at elevated temperatures using coupled thermo-mechanical finite element models, Int. J. Plast. 23 (2007) 841–875.
[23] M. Shah, E. Billur, P. Sartkulvanich, J. Carsley, T. Altan, Cold and warm hydroforming of AA5754-O Sheet: FE simulations and experiments, in: K. Chung, H.N. Han, H. Huh, F. Barlat, M.G. Lee (Eds.) Proceedings of the 8th International Conference and Workshop on Numerical Simulation of 3d Sheet Metal Forming Processes, Amer Inst Physics, Melville, 2011, pp. 690–697.
[24] A.D. Foster, M.S. Mohamed, J. Lin, T.A. Dean, An investigation of lubrication and heat transfer for a sheet aluminium heat, form-quench (HFQ) process, Steel Res. Int. 79 (2009) 133–140.
[25] I.J. Polmear, Light Alloys: Metallurgy of the Light Metals, 3rd ed., Butterworth Heinemann, Melbourne, 1995.
[26] M.S. Mohamed, An investigation of hot forming quench process for AA6082 aluminium alloys, in: Department of Mechanical Engineering, Imperial College London, London, 2010.
[27] J. Lin, T.A. Dean, Modelling of microstructure evolution in hot forming using unified constitutive equations, J. Mater. Process. Technol. 167 (2005) 354–362.
[28] G.B. Burger, A.K. Gupta, P.W. Jeffrey, D.J. Lloyd, Microstructural control of aluminum sheet used in automotive applications, Mater. Charact. 35 (1995) 23–39.
[29] M. Khaleel, H. Zbib, E. Nyberg, Constitutive modeling of deformation and damage in superplastic materials, Int. J. Plast. 17 (2001) 277–296.
[30] B. Li, J. Lin, X. Yao, A novel evolutionary algorithm for determining unified creep damage constitutive equations, Int. J. Mech. Sci. 44 (2002) 987–1002.